JOURNAL OF PLANKTON RESEARCH | VOLUME 34 | NUMBER 9 | PAGES 749–760 | 2012

Spatial and temporal statistics of sea surface temperature and chlorophyll fronts in the California Current

MATI KAHRU[1]*, EMANUELE DI LORENZO[2], MARLENNE MANZANO-SARABIA[3] AND B. GREG MITCHELL[1]

[1]SCRIPPS INSTITUTION OF OCEANOGRAPHY, UNIVERSITY OF CALIFORNIA SAN DIEGO, LA JOLLA, CA, USA, [2]SCHOOL OF EARTH AND ATMOSPHERIC SCIENCES, GEORGIA INSTITUTE OF TECHNOLOGY, 311 FERST DRIVE, ATLANTA, GA 30332-0340, USA AND [3]FACULTAD DE CIENCIAS DEL MAR, UNIVERSIDAD AUTÓNOMA DE SINALOA, MAZATLÁN, SINALOA, MÉXICO

*CORRESPONDING AUTHOR: mkahru@ucsd.edu

Received November 3, 2011; accepted in principle February 1, 2012; accepted for publication February 3, 2012

Corresponding editor: Roger Harris

The statistics of sea-surface fronts detected with the automated histogram method were studied in the California Current using sea-surface temperature (SST) and chlorophyll-*a* concentration (Chl) images from various satellite sensors. Daily maps of fronts were averaged into monthly composites of front frequency (FF) spanning 29 years (1981–2009) for SST and 14 years (1997–2010) for Chl. The large-scale distributions of frontal frequency of both SST (FFsst) and of Chl (FFchl) had a 500–700 km wide band of elevated values (4–7%) along the coast that roughly coincided with the area of increased mesoscale eddy activity. FFsst and FFchl were positively correlated at monthly and seasonal frequencies, but the year-to-year variations were not significantly correlated. The long-period (1 year and longer) variability in FFsst is influenced by the large-scale SST gradient, while at shorter timescales the influence of the Coastal Upwelling Index is evident. In contrast with FFsst, FFchl variability is less related to the coherent large-scale forcing and has stronger sensitivity to local forcings in individual areas. Decadal-scale increasing trends in the frequency of both SST and Chl fronts were detected in the Ensenada Front area (general area of the A-Front study) and corresponded to, respectively, trends towards colder SST and increasing chlorophyll-*a* concentration.

KEYWORDS: fronts; A-Front; sea surface temperature; phytoplankton; chlorophyll; California Current; ocean color; remote sensing

INTRODUCTION

Oceanic fronts, defined as areas of sharp gradients between adjacent water masses (e.g. Legeckis, 1978; Mooers *et al.*, 1978), exist at a wide range of spatial and temporal scales (Belkin, 2009). Fronts are indicators of many oceanographic processes and are sites of increased biological activity affecting all oceanic life forms from microbes to seabirds and marine mammals (e.g. Pingree *et al.*, 1975; Kahru *et al.*, 1984; DiGiacomo *et al.*, 2002; Bost *et al.*, 2009). An example of the factors affecting different marine organisms at fronts is the aggregation of biogenic surfactants, typically on one side of a front (Jessup *et al.*, 2009; Ryan *et al.*, 2010).

Spectacular fronts are created in the California Current System (CCS) by wind-driven upwelling and the subsequent advection of the upwelled water in the form of cold, chlorophyll-rich filaments and the associated eddies (Bernstein *et al.*, 1977; Flament *et al.*, 1985; Strub *et al.*, 1991; Castelao *et al.*, 2006). As pelagic communities and the associated biogeochemical fluxes

doi:10.1093/plankt/fbs010, available online at www.plankt.oxfordjournals.org. Advance Access publication March 1, 2012

in the California Current are often driven by the physical dynamics associated with mesoscale frontal structures (papers in this volume), it is important to understand the long-term dynamics and the statistical properties of fronts and how these may be affected by the interannual and interdecadal climate dynamics. For example, just as upwelling intensity exhibits seasonal and interannual variation (Bakun, 1973), we may find corresponding seasonal and interannual variability in the frontal activity that is associated with upwelling.

The seasonal dynamics of sea-surface temperature (SST) fronts in the California Current were studied by (Castelao *et al.*, 2006). Using geostationary satellite data for the period 2001–04, they showed that the probability of detecting a front was associated with the seasonal development of coastal upwelling: it peaked in the summer and was at its minimum during the winter. Here we observe the statistics of SST fronts during a much longer time period (1981–2009) and try to detect trends. As SST fronts and the associated physical dynamics are expected to influence the biology of the California Current, we compare the spatial, seasonal and interannual statistics of SST fronts with the fronts in surface chlorophyll-*a* concentration detected with ocean color satellites. In order to overcome the limitations imposed by the missing satellite data due to clouds, we use compositing front detection results from multiple images and multiple satellites.

DATA AND METHODS

Automated methods of front detection became important with the ease of access to satellite data, primarily of SST (Holyer and Peckinpaugh, 1989). The histogram method developed by Cayula and Cornillon (Cayula and Cornillon, 1992) has excelled in tests (Cayula *et al.*, 1991) and has been applied extensively to objective mapping of SST fronts (Kahru *et al.*, 1995; Ullman and Cornillon, 1999; Diehl *et al.*, 2002; Belkin *et al.*, 2009). The basic idea of the histogram method is to search for bimodality of histograms calculated for overlapping windows of the image. The method is not limited to SST and can also be applied to other types of satellite images, such as of chlorophyll-*a* concentration (Chl) (e.g. Bontempi and Yoder, 2004). The spatial variability structure of Chl and SST images are different. Chl fronts have been associated with the 'peak' model (where the maximum occurs at the front). In contrast, SST fronts typically follow the 'ramp' or 'step' model (Belkin and O'Reilly, 2009). However, with sufficient spatial resolution, what looks like a 'peak' front at low resolution often becomes a 'ramp' front at high resolution and is easily detectable with the histogram method. We used the Cayula and Cornillon (Cayula and Cornillon, 1992) single-image edge detection method with a fixed window size of 32 × 32 pixels. We also tested the variable window size modification (Diehl *et al.*, 2002), but found it to be too sensitive to small-scale features (results not shown).

The spatial and temporal coverage by visible and infrared satellite images is severely limited by cloud cover. Cloud-free images of a single satellite pass covering large areas are rarely available, and a tempting approach is to use images composited over a longer time period, e.g. 8 days or a month. However, composite images have artificial fronts created by the compositing process itself and may be missing real fronts that become undetectable from the smoothing and averaging over multiple images. It is therefore best not to use composited images for front detection. We therefore used daily SST and Chl images and composited the fronts detected into a mean front frequency (FF) averaged over monthly periods. The FF value gives the estimated probability that a pixel is classified as a front pixel. FF is estimated as the ratio of the number of times a pixel was determined as a front pixel to the number of times the pixel had valid data.

For SST, we used the daily 4-km AVHRR Pathfinder 5 data set (http://www.nodc.noaa.gov/SatelliteData/pathfinder4km/) described by Casey *et al.* (Casey *et al.*, 2010). These data are mapped to a standard global map in geographic projection. In total, 13 053 daily SST images covering 29 years (1981–1984 using version 5.1 and 1985–2009 using version 5.0) were analyzed and used for front detection. The daily data sets were first screened for low-quality data and only pixels with quality level 4 and above were included. Fronts were detected in the daily images, and the average front frequency of SST (FF_{sst}) was estimated for each pixel over a month as the ratio of the count of front detections to the count of valid data. For example, if a particular pixel was cloud-free (valid) in 20 daily images and was detected as a front pixel in 2 of them, the FF was 0.1 or 10%. The monthly FF values of individual pixels were averaged spatially over certain spatial domains of adjacent pixels (selected areas or 'masks'), and the means were plotted as time series.

For chlorophyll-*a* concentration (Chl, mg m^{-3}), we obtained level-2 data (full resolution, unmapped) from NASA's Ocean Color website (http://oceancolor.gsfc.nasa.gov/) and ESA's MERIS Catalogue and Inventory (http://merci-srv.eo.esa.int/merci/welcome.do; data available after registration at http://eopi.esa.int/esa/esa?cmd=aodetail&aoname=Registration). The Chl

data sets calculated with the standard Case 1 algorithms (O'Reilly *et al.*, 1998; Morel and Antoine, 2007; Morel *et al.*, 2007) were mapped to an Albers conic equal area map with 1-km^2 pixel size (methods described in http://spg.ucsd.edu/Satellite_Projects/CAL/). The latest versions of the processed data were used: 2010.1 for SeaWiFS data (1997–2010), 2009.1 for MODIS Aqua (MODISA, 2002–10) and 5.0 for MERIS (2003–10). To be compatible with the 4-km SST images, the 1-km Chl images were reduced four times (by averaging neighboring four pixels into one), and the front detection was applied to $\log_{10}$-transformed daily Chl maps at 4-km resolution. Front maps determined from three individual sensors (SeaWiFS, MODISA, MERIS) were pooled by adding the counts of valid and detected front pixels, and the merged monthly Chl front frequency (FFchl) was calculated using the pooled counts.

SST anomaly was calculated by subtracting the mean climatological monthly value from the monthly mean value of each pixel. Chl anomaly was calculated as a ratio of the current monthly value to the mean climatological monthly value, e.g. anomaly of 0.5 means half of the normal value.

The analysis of the interannual signals and of their connection to large-scale patterns of variability was conducted using the monthly anomalies of sea level pressure (SLP) from the NCEP Reanalysis II (Kalnay *et al.*, 1996) and SST from the NOAA Reanalysis (Smith and Reynolds, 2004). The monthly anomalies were computed by removing the respective climatological monthly means.

The monthly Coastal Upwelling Index (CUI, $m^3\ s^{-1}\ 100\ m^{-1}$ coastline) values for multiple latitudes of the North American coastline were obtained from the NOAA Pacific Fisheries Environmental Laboratory website (http://las.pfeg.noaa.gov/las6_5/servlets/dataset?catitem=1673).

Weekly gridded maps of the sea level anomaly (SLA) merged from multiple satellites by AVISO (Ducet *et al.*, 2000) were used to evaluate eddy variability. The large-scale SLA is computed by applying a spatial box filter of 400 km on the SLA data, and the mesoscale SLA is defined as the residual after subtracting the large-scale SLA from the AVISO SLA.

The significance of the correlation coefficients between time series was estimated from the Probability Distribution Functions (PDFs) of the correlation coefficient of the two time series with the same autoregression coefficients as estimated from the original signals. The PDFs were computed numerically by generating 1500 realizations of the correlation coefficients for the two random autocorrelated time series.

RESULTS AND DISCUSSION

Spatial patterns of the distribution of fronts

Examples of detected SST and Chl fronts overlaid on 1-km mapped MODISA and MERIS images (Fig. 1) show that the major Chl fronts are associated with upwelling filaments resulting from coastal upwelling. Due to rapid growth of phytoplankton in these nutrient-rich waters, the filaments are enriched in Chl. The high-Chl filaments can be followed as they are advected in the southern and south-western directions. In this region, major SST fronts are always coincident with Chl fronts, but the contrast across a front is different for SST and Chl; therefore, not all SST fronts are detected as Chl fronts and vice versa. Examples of the monthly composited FF for both SST (FFsst) and Chl (FFchl) are shown in Fig. 2. Images of the monthly averaged FFsst appear noisier than those of the corresponding Chl fronts. However, the correlations of FFsst with the large-scale variability and upwelling winds on interannual timescale are higher than those with FFchl (see below). The

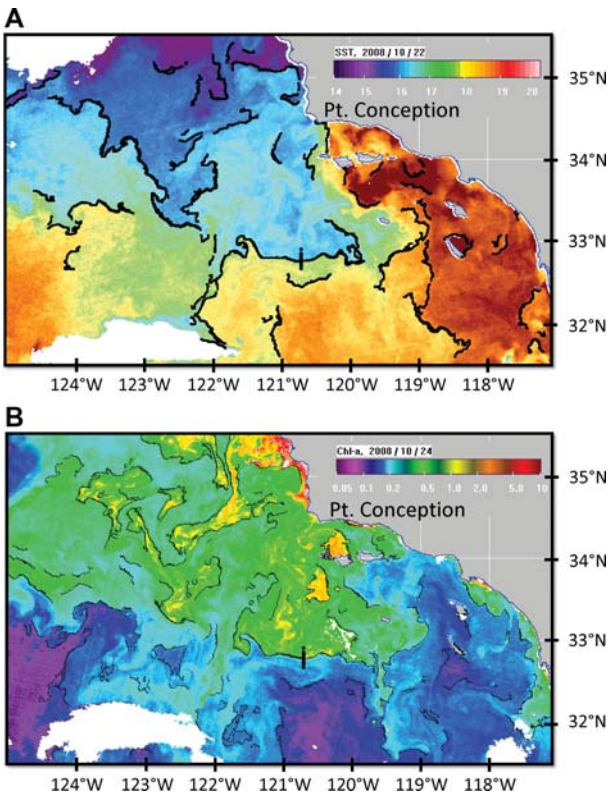

Fig. 1. Examples of detected fronts, shown as black contours on top of a SST image (**A**, MODIS Aqua, 22 October 2008) and a chlorophyll-*a* (mg m^{-3}) image (**B**, MERIS, 24 October 2008). White areas are clouds. Black vertically spaced dots across a front near the center show the locations of CTD-UVP5/Bongo stations between cycles 5 and 6 of the A-Front study.

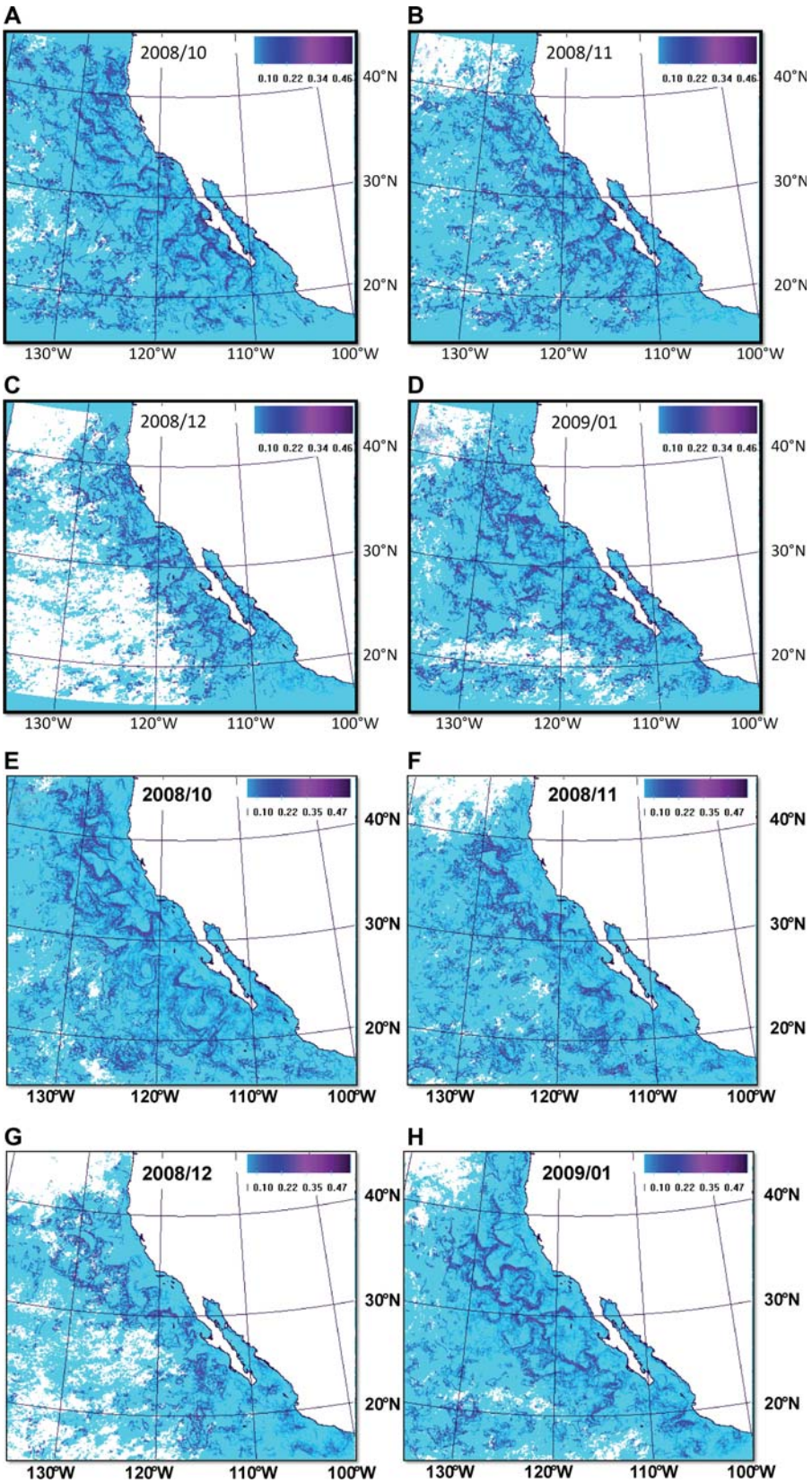

Fig. 2. Monthly composites of FF from October 2008 to January 2009. White areas have less than three valid pixels during the monthly period and are not used. (**A**–**D**) SST FF; (**E**–**H**) Chl FF.

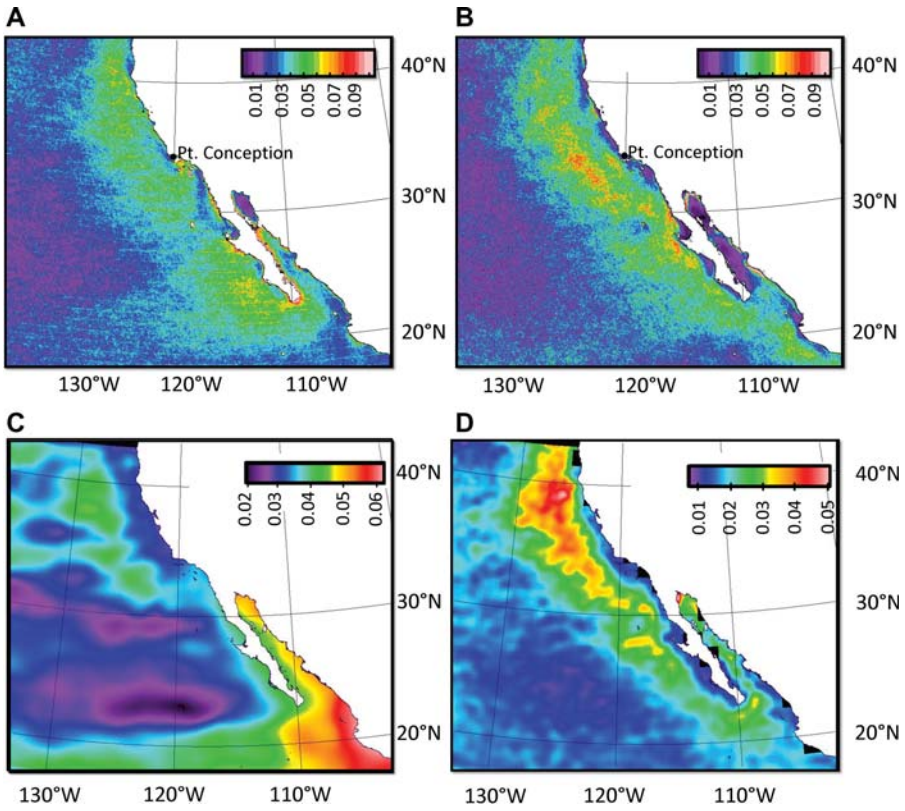

Fig. 3. Overall mean FF for SST (**A**, 1981–2009) and Chl (**B**, 1997–2010). Variance of the sea level height anomaly (m^2) separated into the large-scale component (**C**) and mesoscale (**D**) component.

monthly FFchl patterns (Fig. 2E and F) show that the major large-scale Chl fronts are quite consistent in space and that their movement can be followed by the adjacent quasi-parallel curves. The actual number of days that a particular structure is observed is variable and depends on the number of cloud-free pixels per month. Due to frequent cloud cover, large offshore areas may have less than three valid pixels per month. For those pixels, FF statistics were not calculated.

The overall mean frontal frequency of both SST and Chl averaged over monthly FF (1981–2009 for SST and 1996–2010 for Chl) has a band of elevated values (4–7%) along the coast that is approximately 500–700-km wide (Fig. 3A and B). FFchl, in particular, often showed local minima near the coast. This does not mean that there is less variability near the coast but rather that the variability is at shorter scales and fronts are not detected using the selected settings of the algorithm. The center of gravity of the FFsst maxima is off the southern Baja California peninsula, whereas the center of gravity of FFchl is more to the north, off central California. Within the wide band of increased frontal frequency, FFchl has a major core of maxima at about 300 km from the coast in central and southern California and narrower cores of maxima at about 100 km from Point Conception and off the coast of the central Baja California peninsula. The wide bands of high frontal frequencies in both FFsst and FFchl correspond to the region of high mesoscale eddy activity as shown by satellite SLA variance maps (Fig. 3C and D), suggesting that both upwelling filaments and eddy activity play a role in the statistics of FFsst and FFchl.

The highest FF values (>10%) are in the Gulf of California, related to the bottom topography, and are near the coast, parallel to the coastline. Those areas of highest FF in the Gulf of California are different for FFsst and FFchl (Fig. 3A and B). The highest FFchl values are near the northern end of the Gulf of California and along its south-eastern coast, whereas the maxima in FFsst are along the north-western coast. The lowest FF values (<0.5%) are located in the central parts of the Gulf of California (only the northern basin for FFsst) and are probably caused by the strong vertical stratification there due to intense surface heating.

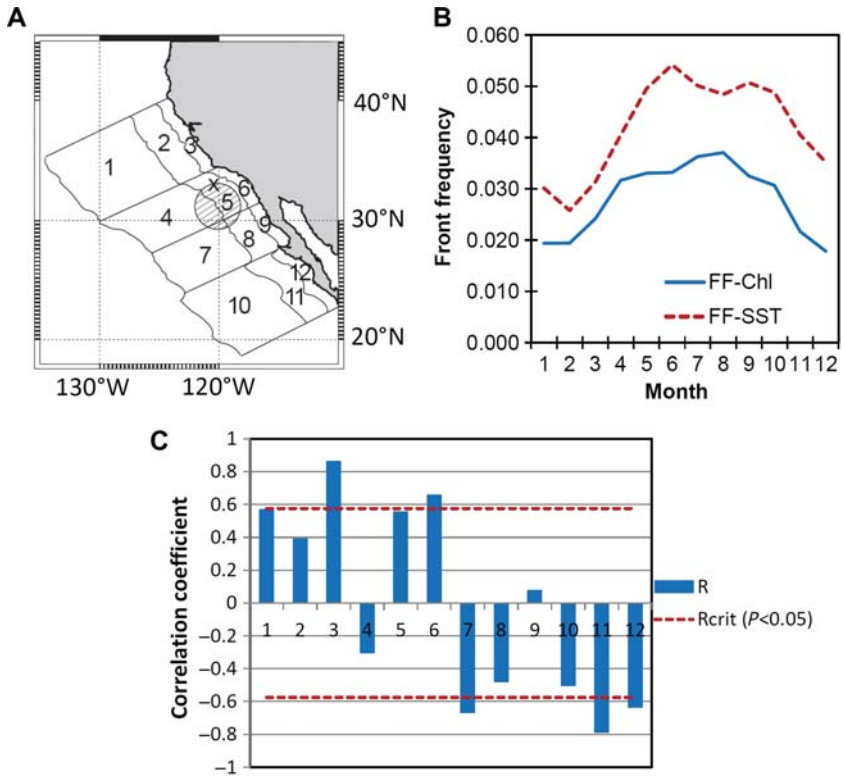

Fig. 4. (**A**) Grid of 12 selected areas for calculating averaged time series in bands parallel and across the mean coastline: coastal (0–100 km), transition (100–300 km) and offshore (300–1000 km). The striped circle shows the approximate location of the Ensenada Front. (**B**), Mean annual cycles of SST and Chl front frequencies in the northern coastal area (area 3). (**C**) Correlation coefficients (R) between the mean annual cycles of the frontal frequencies of SST and Chl in the 12 selected areas. Dashed red lines indicate the critical values of R at $P < 0.05$.

Annual cycles of FF

In order to analyze large-scale spatial differences in front frequencies, we divide the whole domain into a grid of 12 areas from offshore (approximate distance from coast 300–1000 km) through transition (100–300 km) to coastal (0–100 km), and from north to south as Central California (areas 1–3), Southern California (areas 4–6), Northern Baja (areas 7–9) and Southern Baja (areas 9–12) (Fig. 4A). This grid has been used in the past (e.g. Kahru and Mitchell, 2001) and derives from the work of Lynn and Simpson (Lynn and Simpson, 1987) who showed that the variability structure of dynamic height in the California Current can be divided into offshore, transition and coastal bands that are roughly parallel to the coast.

The mean annual cycle of both FFsst and FFchl is weak offshore and stronger in the transition and coastal areas (0–300 km). In the northern part of the domain, the annual cycles of FFsst and FFchl tend to be positively correlated with maxima from June to August (Fig. 4B) and minima in winter (December to February). In the southern half of the domain, the annual cycles of FFsst and FFchl tend to be negatively correlated (Fig. 4C), with FFchl maxima occurring in the summer but (weak) FFsst maxima occurring in the winter. Castelao *et al.* (Castelao *et al.*, 2006) also observed weak seasonality in FFsst off northern Baja California. It is likely that the suppressed FFsst in the summer is caused by the increased vertical stratification due to weaker winds and intense solar heating in the summer. SST fronts are often masked during the summer due to increased vertical stratification near the surface, whereas Chl fronts are less affected (Pegau *et al.*, 2002; Takahashi and Kawamura, 2005).

The mean annual cycle of FFchl is positively correlated ($R = 0.84–0.90$, $P < 0.01$, plots not shown) with the mean annual CUI in the coastal 100-km band, except off southern Baja California, where the correlation is insignificant ($R = 0.55$, $P > 0.05$). The correlation between the mean annual cycles of FFsst and CUI is variable and changes from positive in some areas (area 3) to negative in others (area 6).

FF in the Ensenada front area

Time series of frontal frequency were examined in the Ensenada Front area (Haury *et al.*, 1993), just south of

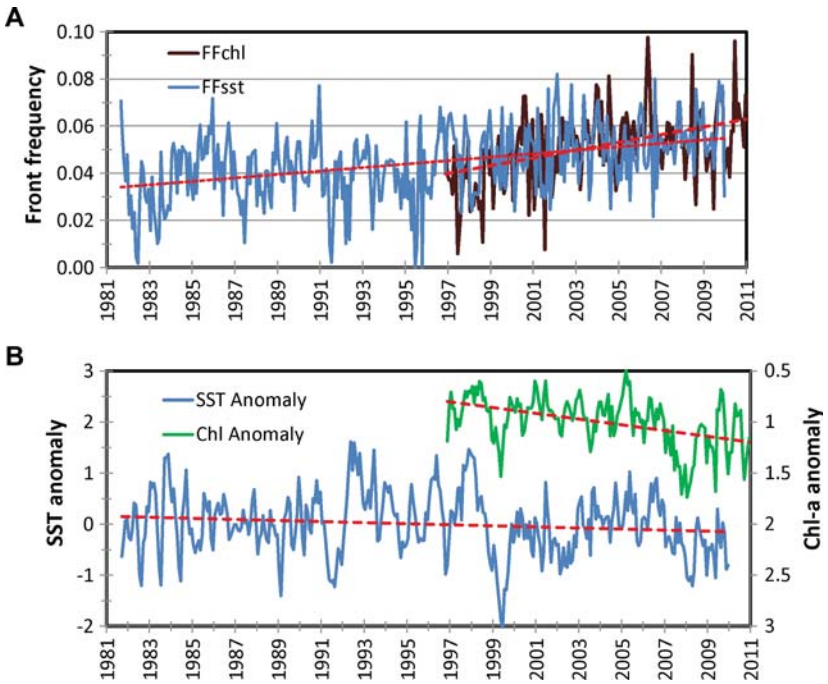

Fig. 5. (**A**) Time series of monthly front frequencies of SST (blue line) and of Chl (brown) in the Ensenada Front area (see Fig 4A). Both time series show statistically significant ($P < 0.01$) increasing trends. (**B**) Trends in monthly anomalies of SST (blue, °C, left axis) and of Chl (green, right axis) in the same area. Note that Chl anomaly is increasing downwards.

the A-Front study area (Fig. 4A). We averaged FF and other variables over a circular domain with a diameter of ~375 km, centered at 31.31°N; 120.23°W. While some temporal features in FFchl were coherent with similar features in FFsst, others were not. The overall correlation between FFsst and FFchl was weak, but significant ($R = 0.30$, $P < 0.01$). We detected statistically significant (*F*-test, $P < 0.01$) increasing temporal trends (Fig. 5) for both FFsst (slope = 0.0007, 1981–2009) and FFchl (slope = 0.0016, 1997–2010). The mean slopes for the overlapping period (1996–2009) were, respectively, 0.00073 year^{-1} for FFsst and 0.0016 year^{-1} for FFchl (both $P < 0.01$). Significant trends were also detected in SST monthly anomalies (decrease with a slope of −0.0105°C year^{-1}) and Chl anomalies (increase with a slope of 0.0282 year^{-1}).

Correlations with CUI

The time series of FFchl in coastal areas were positively correlated with the CUI. The magnitude of the correlation between FFchl and CUI at the same approximate latitude changes from stronger to weaker from the northern areas to the southern areas (from $R = 0.47$, $P < 0.01$ in area 3 to $R = 0.27$, $P < 0.01$ in area 12). The correlation of the FFsst time series with CUI (not shown) is also positive but weaker and has a similar tendency to weaken from north to south. However, CUI at 33°N (CUI-33) has a strong positive correlation with satellite-derived chlorophyll-*a* concentration in a band of about 100-km wide along the whole West coast down to 22°N and negative correlation with Chl offshore (Fig. 6A). The correlation of CUI-33 with FFchl is positive in both the nearshore and offshore domains, while the correlation in the transition zone is insignificant (Fig. 6B).

Interannual and large-scale structure

To assess interannual variability of the frontal frequencies and examine the large-scale coherence of the frontal signals, we removed the annual cycle from each of the FFsst and FFchl time series for the 12 regions of Fig. 4A. We then defined the average FF time series by averaging the FF indices of all the 12 areas, and correlated the average FF time series with FF of the individual areas. The FFsst signals exhibit more large-scale coherence across all of the regions, with the average significant correlation of $R = 0.63$ (Fig. 7A). These correlations are stronger in the northern regions and weaker in the south. For the FFchl, the large-scale coherence is not as strong as for FFsst, and the average correlations between the mean FFchl index and the individual area FFchl is $R = 0.42$, with higher values in the southern

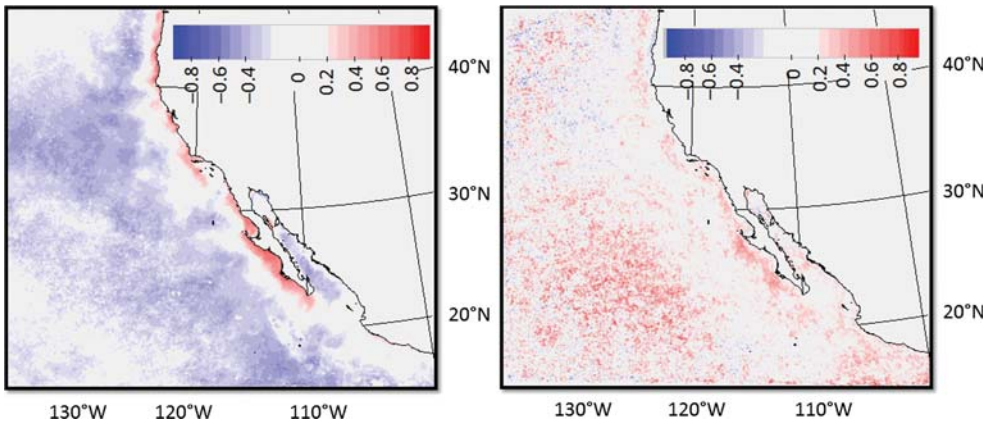

Fig. 6. Spatial correlation of the CUI at 33°N with (**A**) satellite-derived chlorophyll-*a* concentration and (**B**) Chl front frequency (FFchl). Blue colors show negative and red colors positive correlation. Low and statistically insignificant ($P > 0.05$) correlations are white.

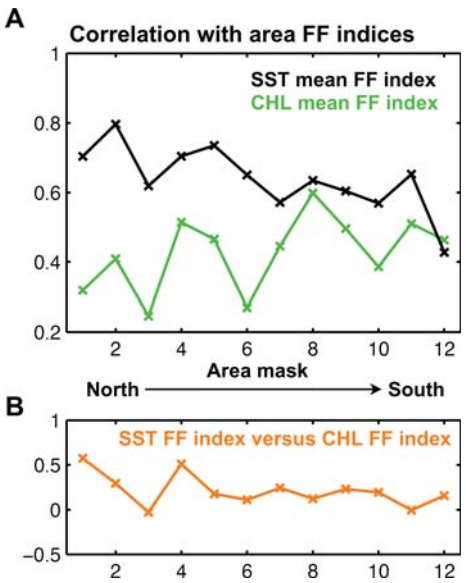

Fig. 7. (**A**) Correlation of the average FF index with the individual area FF index. The average FF index is computed by averaging the FF indices of all the areas. (**B**), Correlation of FFsst and FFchl indices in each area after removing the mean annual cycle (average correlation is $R = 0.3$).

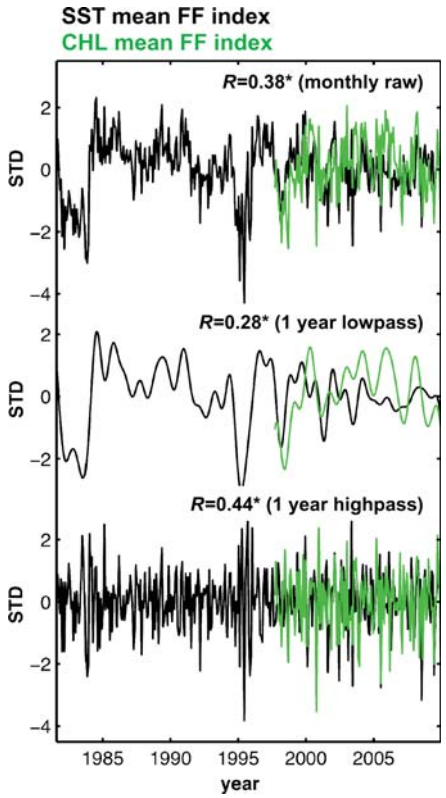

Fig. 8. Correlation between the mean FF indices for SST and Chl. The mean index is computed by averaging the FF index of all the 12 areas. The correlations are computed between the raw mean indices and for the 1 year low-pass and high-pass versions to establish the frequency bands where the SST and Chl fronts share most of their variance.

regions. This indicates that frontal frequencies in Chl have a stronger sensitivity to local controls or forcing in the individual regions and are less connected to the coherent large-scale forcing. It is evident that most of the correlation between FFsst and FFchl in coastal areas (e.g. Fig. 4B) comes from their similar annual cycles. After removing the mean annual cycle, the correlations between FFsst and FFchl are quite different (cf. Fig. 4C and Fig. 7B), and the offshore areas 1 and 4 have the highest correlation.

A comparison between the interannual variability of the areal average frontal frequency indices for SST and Chl (Fig. 8) shows significant correlation $R = 0.38$ ($P < 0.05$). However, a closer look at the variability in the two time series reveals that year-to-year variations in SST and Chl frontal frequencies (1-year lowpass) are

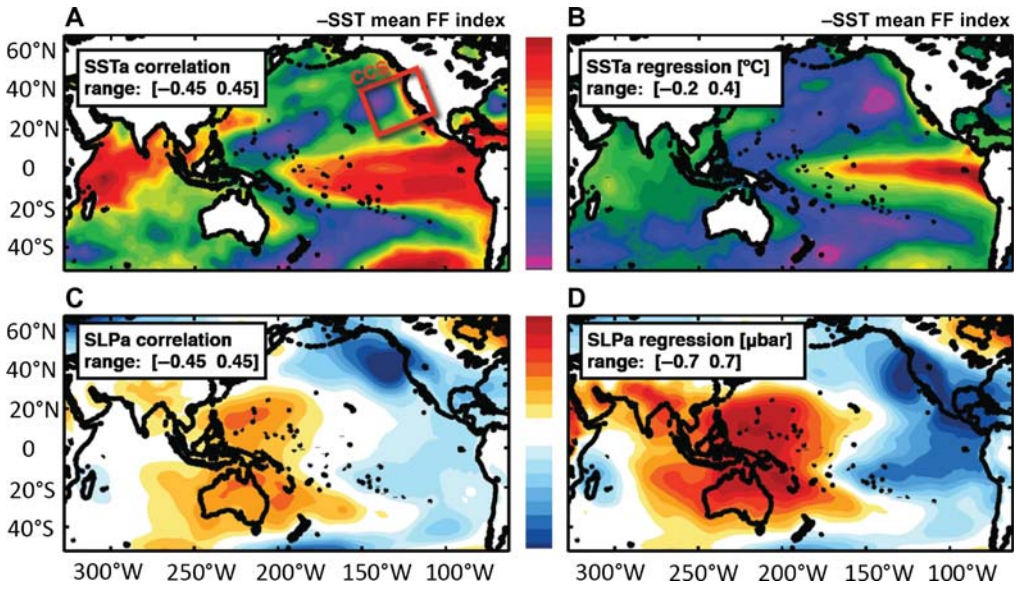

Fig. 9. The SST-derived mean frontal frequency index averaged over all the 12 areas is used with a negative sign (−SST mean FF index) to produce correlation and regression maps with the NOAA SST anomalies (**A** and **B**) and NCEP SLP anomalies (**C** and **D**).

not significantly correlated. The bulk of the correlation comes from the high frequency sub-annual variability (monthly timescale) of the SST and Chl fronts, which are significantly correlated ($R = 0.44$; $P < 0.01$).

To explore the connection of frontal frequencies with large-scale dynamics and forcings, we examined the correlation and regression maps of the mean FFsst index with the large-scale NOAA SST and NCEP SLP anomalies (Fig. 9). We focused on FFsst because it exhibited a larger degree of coherence across all areas when compared with FFchl. The SST correlation and regression maps (Fig. 9A and B) reveal a pattern that is similar to the SST anomalies associated with El Niño. Indeed, the mean FFsst index is negatively correlated with the Multivariate ENSO Index (Wolter and Timlin, 1998), with $R = -0.34$ ($P < 0.01$). The SLP correlation and regression maps also show a spatial structure resembling the El Niño signal. Correlations with other indices of large-scale variability such as the Pacific Decadal Oscillation (Mantua *et al.*, 1997) and the North Pacific Gyre Oscillation (Di Lorenzo *et al.*, 2008) are not significant. To better understand the forcing dynamics of FFsst, we examined the correlation maps over the CCS region. We found that during the time of low FFsst, the SST is characterized by warmer waters along the coast and a stronger than usual cross-shelf gradient in SST (Fig. 9A). This result suggests that both changes in upwelling associated with the warm/cold coastal SST and changes in the large-scale SST cross-shelf gradient may exert a direct control on the statistics of SST fronts on the CCS scale.

Stronger coastal upwelling winds induce an intensification of the coastal jet as well as secondary upwelling within the mesoscale eddies. Both of these dynamics can lead to an enhancement of filaments and frontal structures in the CCS. To quantify the role of upwelling winds on frontal frequency statistics, we correlated the monthly CUI anomalies over the CCS with the mean FFsst index (Fig. 10A). This shows that a significant correlation exists between the winds and frontal frequency in the high-frequency band of monthly timescales. However, on year-to-year timescales, the frequency of the SST fronts does not follow the changes in upwelling winds but rather is correlated with changes in the large-scale cross-shelf gradient in SST. This is evident from a correlation analysis of the mean FFsst index with an index that measures the large-scale gradient of SST in the CCS between latitudes 32−40°N (Fig. 10B). In the CCS, changes in the cross-shelf SST gradient may be driven by coastally trapped waves of tropical origin (e.g. El Niño) and large-scale changes in upwelling as evident from the SLP anomalies of Fig. 9C and D. We hypothesize that, during times of stronger mean cross-shelf SST gradients in the CCS, the mesoscale eddies are more efficient in creating filaments with stronger SST contrasts, leading to the detection of stronger and more frequent frontal features. A similar analysis conducted for the mean FFchl index did not lead to any significant correlations. In addition, the high-frequency variability of the mean FFchl index does not covary with the high-frequency variability of the large-scale upwelling winds, although they do covary on the annual cycle. The lack of significant correlations

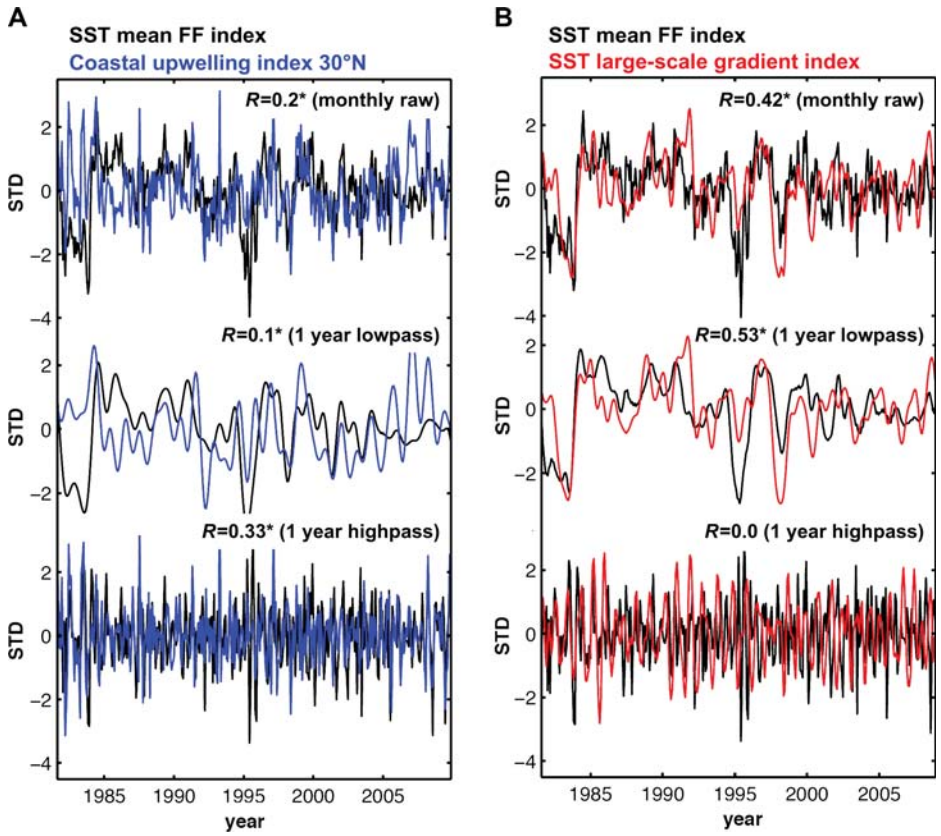

Fig. 10. Correlation of the SST mean FF index with the CUI at 30°N (**A**) and with the SST cross-shore gradient index (**B**). The SST mean FF index is computed by averaging the FF index across all 12 areas.

between the FFchl index and these large-scale physical indices (e.g. upwelling winds and cross-shelf SST gradient index) lends further support to the suggestion that Chl frontal structures are more sensitive to local forcing dynamics. One possible explanation of the different sensitivities of the Chl and SST frontal statistics may be the linear versus nonlinear response of the SST and Chl fields to external forcing. As an example, with a sudden intensification of the winds over a frontal structure, the changes in upwelling at the frontal structure will produce a linear enhancement of the SST gradients. However, the changes in nutrient upwelling (linear) will produce a change in biological productivity and in the Chl signature that is exponential in nature (nonlinear). This nonlinear behavior enhances the sensitivity of the Chl frontal features to high frequency local wind events, which may not be captured when using large-scale means of the wind field.

SUMMARY

We created a consistent quantitative time series of the sea-surface fronts detected from satellite-detected data sets of SST and Chl for the domain of the California Current (16–45°N, 140–100°W) that is 29 years long for SST and 14 years long for Chl. While the methods used here for front detection are objective, the results depend on a multitude of details of application and on the type and quality of satellite data being used. In spite of these shortcomings, we believe that the time series of frontal frequencies are objective characteristics of the system. Because of the extensive and frequent cloud cover, we had to composite (average) the daily distributions of fronts into monthly mean distributions normalized by the number of cloud-free images. These monthly time series of front frequencies have a significant error component due to missing data, and the error is bigger offshore where the frequency of cloud-free days is lower.

In this region, major SST fronts always coincide with Chl fronts, but the across-front contrast is variable for SST and Chl. Therefore, not all SST fronts are detected as Chl fronts, and vice versa. Compounded with the different coverage of various satellite sensors, this produces different spatial and temporal statistics for the SST and Chl fronts. While both SST and Chl fronts are affected

by upwelling and mesoscale eddy dynamics, Chl fronts have a stronger sensitivity to local controls or forcing and are less connected to the coherent large-scale variability of SST and SLP anomalies. Large-scale changes in the cross-shelf SST gradient in the CCS, driven by coastally trapped waves of tropical origin (e.g. El Niño) and large-scale upwelling, were found to track the year-to-year changes in the SST frontal frequency, but they had no significant correlation with Chl frontal frequency. The year-to-year variations between FFsst and FFchl are therefore not significantly correlated, while seasonal and subseasonal variations are correlated.

Significant decadal-scale trends were detected in the Ensenada Front area where front frequencies of both SST and chlorophyll-*a* have increased together with trends toward higher chlorophyll-*a* concentration and colder SST. Increasing frontal frequency due to the increased number of filaments and eddies is likely indicating increased nutrient input into the upper layer that is producing the increase in chlorophyll-*a*. All these trends are consistent with the observed increase in upwelling-favorable winds and wind-driven coastal upwelling (García-Reyes and Largier, 2010).

ACKNOWLEDGEMENTS

Satellite data were provided by the NASA Ocean Biology Processing Group, ESA MERIS team and NOAA National Oceanographic Data Center.

FUNDING

This work was supported by the NASA Ocean Biology and Biogeochemistry Program and the CCE-LTER program, supported by NSF. We also acknowledge the support of NSF (grants OCE-1026607, GLOBEC-0606575), POBEX project (www.pobex.org), the University of California Institute for Mexico and the United States (UC MEXUS) and Consejo Nacional de Ciencia y Tecnología, Mexico (CONACYT).

REFERENCES

Bakun, A. (1973) Coastal upwelling indices, west coast of North America, 1946–71. *Spec. Sci. Rep.*, **671**, 103. Natl. Mar. Fish. Serv., Seattle, Wash.

Belkin, I. M. (2009) Observational studies of oceanic fronts. *J. Mar. Syst.*, **78**, 317–318.

Belkin, I. M., Cornillon, P. C. and Sherman, K. (2009) Fronts in Large Marine Ecosystems. *Prog. Oceanogr.*, **81**, 223–236.

Belkin, I. M. and O'Reilly, J. E. (2009) An algorithm for oceanic front detection in chlorophyll and SST satellite imagery. *J. Mar. Syst.*, **78**, 319–326.

Bernstein, R. L., Breaker, L. and Whritner, R. (1977) California Current eddy formation: ship air and satellite results. *Science*, **195**, 353–359.

Bontempi, P. S. and Yoder, J. A. (2004) Spatial variability in SeaWiFS imagery of the South Atlantic bight as evidenced by gradients (fronts) in chlorophyll a and water-leaving radiance. *Deep-Sea Res. II*, **51**, 1019–1032.

Bost, C. A., Cotte, C., Bailleul, F. *et al.* (2009) The importance of oceanographic fronts to marine birds and mammals of the southern oceans. *J. Mar. Syst.*, **78**, 363–376. doi:10.1016/j.jmarsys.2008.11.022.

Casey, K. S., Brandon, T. B., Cornillon, P. *et al.* (2010). *The past, present and future of the AVHRR Pathfinder SST program, in Oceanography from Space: Revisited*. In Barale, V., Gower, J. F. R. and Alberotanza, L. (eds), Springer. DOI: 10.1007/978-90-481-8681-5_16.

Castelao, R. M., Mavor, T. P., Barth, J. A. *et al.* (2006) Sea surface temperature fronts in the California Current System from geostationary satellite observations. *J. Geophys. Res.*, **111**, doi:10.1029/2006JC003541.

Cayula, J. -F. and Cornillon, P. (1992) Edge detection algorithm for SST images. *J. Atmos. Oceanic Technol.*, **9**, 67–80.

Cayula, J. -F., Cornillon, P., Holyer, R. J. *et al.*. (1991) Comparative study of two recent algorithms designed to process sea-surface temperature fields. *IEEE Trans. Geosci. Remote Sens.*, **GE-29**, 175–177.

Diehl, S. F., Budd, J. W., Ullman, D. *et al.* (2002) Geographic window sizes applied to remote sensing sea surface temperature front detection. *J. Atmos. Oceanic Technol.*, **19**, 1105–1113.

DiGiacomo, P. M., Hamner, W. M., Hamner, P. P. *et al.* (2002) Phalaropes feeding at a coastal front in Santa Monica Bay, California. *J. Mar. Syst.*, **37**, 199–212, doi:10.1016/S0924-7963(02)00202-6.

Di Lorenzo, E., Schneider, N., Cobb, K. M. *et al.* (2008) North Pacific Gyre Oscillation links ocean climate and ecosystem change. *Geophys. Res. Lett.*, **35**, doi:10.1029/2007GL032838.

Ducet, N., Le Traon, P.-Y. and Reverdin, G. (2000) Global high resolution mapping of ocean circulation from TOPEX/Poseidon and ERS-1/2. *J. Geophys. Res.*, **105**, 19477–19498.

Flament, P., Armi, L. and Washburn, L. (1985) The evolving structure of an upwelling filament. *J. Geophys. Res.*, **90**, 11765–11778. doi:10.1029/JC090iC06p11765.

García-Reyes, M. and Largier, J. (2010) Observations of increased wind-driven coastal upwelling off central California. *J. Geophys. Res.*, **115**, C04011, doi:10.1029/2009JC005576.

Haury, L. R., Venrick, E. L., Fey, C. L. *et al.* (1993) The Ensenada Front: July 1985. *CalCOFI Rep.*, **34**, 69–88.

Holyer, R. J. and Peckinpaugh, S. H. (1989) Edge detection applied to satellite imagery of the oceans. *IEEE Trans. Geosci. Rem. Sens.*, **27**, 46–56.

Jessup, D. A., Miller, M. A., Ryan, J. P. *et al.* (2009) Mass stranding of marine birds caused by a surfactant-producing red tide. *PLoS ONE*, **4**, E4550, doi:10.1371/journal.pone.0004550.

Kahru, M., Elken, J., Kotta, I. *et al.* (1984) Plankton distributions and processes across a front in the open Baltic Sea. *Mar. Ecol. Prog Ser.*, **20**, 101–111.

Kahru, M., Håkansson, B. and Rud, O. (1995) Distributions of the sea-surface temperature fronts in the Baltic Sea as derived from satellite imagery. *Cont. Shelf Res.*, **15**, 663–679.

Kahru, M. and Mitchell, B. G. (2001) Seasonal and nonseasonal variability of satellite-derived chlorophyll and colored dissolved organic matter concentration in the California Current. *J. Geophys. Res.*, **106**, 2517–2529. doi:10.1029/1999JC000094.

Kalnay, E., Kanamitsu, M., Kistler, R. *et al.* (1996) The NCEP/NCAR 40-year reanalysis project. *Bull. Am. Meteorol. Soc.*, **77**, 437–471.

Legeckis, R. (1978) A survey of worldwide sea surface temperature fronts detected by environmental satellites. *J. Geophys. Res.*, **83**, 4501–4522.

Lynn, R. J. and Simpson, J. J. (1987) The California Current system: the seasonal variability of its physical characteristics. *J. Geophys. Res.*, **92**, 12947–12966.

Mantua, N. J., Hare, S. R., Zhang, Y. *et al.* (1997) A Pacific decadal climate oscillation with impacts on salmon. *Bull. Am. Meteorol. Soc.*, **78**, 1069–1079.

Mooers, C. N., Flagg, K. and Boicourt, W. C. (1978) Prograde and retrograde fronts. In Bowman, M. and Esias, W. (eds), *Oceanic Fronts in Coastal Processes*. Springer, New York, pp. 43–58.

Morel, A. and Antoine, D. (2007) Pigment index retrieval in Case 1 waters. MERIS level 2 algorithm theoretical basis document. *ATBD2.9, ESA Doc*. No. PO-TN-MEL-GS-0005 Issue 4.

Morel, A., Huot, Y., Gentili, B. *et al.* (2007) Examining the consistency of products derived from various ocean color sensors in open ocean (Case 1) waters in the perspective of a multi-sensor approach. *Remote Sens. Environ.*, **111**, 69–88.

O'Reilly, J. E., Maritorena, S., Mitchell, B. G. *et al.* (1998) Ocean color chlorophyll algorithms for SeaWiFS. *J. Geophys. Res.*, **103**, 24937–24953.

Pegau, W. S., Boss, E. and Martinez, A. (2002) Ocean color observations of eddies during the summer in the Gulf of California. *Geophys. Res. Lett.*, **29**, 1295. doi:10.1029/2001GL014076.

Pingree, R. D., Pugh, P. R., Holligan, P. M. *et al.* (1975) Summer phytoplankton blooms and red tides along tidal fronts in the approaches to the English Channel. *Nature*, **258**, 672–677. doi:10.1038/258672a0.

Ryan, J. P., Fischer, A. M., Kudela, R. M. *et al.* (2010) Recurrent frontal slicks of a coastal ocean upwelling shadow. *J. Geophys. Res.*, **115**, doi:10.1029/2010JC006398.

Smith, T. M. and Reynolds, R. W. (2004) Improved extended reconstruction of SST (1854–1997). *J. Climate*, **17**, 2466–2477.

Strub, P. T., Kosro, P. M. and Huyer, A. (1991) The nature of the cold filaments in the California Current System. *J. Geophys. Res.*, **96**, 14743–14768.

Takahashi, W. and Kawamura, H. (2005) Detection method of the Kuroshio front using the satellite-derived chlorophyll-a images. *Remote Sens. Environ.*, **97**, 83–91.

Ullman, D. S. and Cornillon, P. C. (1999) Surface temperature fronts off the East Coast of North America from AVHRR imagery. *J. Geophys. Res.*, **104**, 23459–23478.

Wolter, K. and Timlin, M. S. (1998) Measuring the strength of ENSO events - how does 1997/98 rank? *Weather*, **53**, 315–324.